# Gyrotropic sphere: Selected examples of resonance spectra

J. R. Dixon, Jr.* and J. K. Furdyna
*Department of Physics, Purdue University, West Lafayette, Indiana 47907*
(Received 7 August 1978)

The formal solution to the interaction of a plane electromagnetic wave with a gyrotropic sphere, which was developed by Ford and Werner in the preceding paper, is carried out numerically. We discuss the resonance spectra of two free-carrier systems made gyrotropic by the presence of a dc magnetic field. The first system is a gyrotropic sphere consisting of a single-carrier $n$-type semiconductor with microwaves incident on the sphere. Such a system displays a series of magnetic and a series of electric dimensional resonances that are associated with all multipole orders of the scattering coefficients. The resonant internal magnetic and displacement field patterns are similar in some respects to their isotropic (Mie) sphere counterparts. The resonant internal electric field patterns, however, differ markedly from those of Mie resonances, since the electric fields in the gyrotropic sphere are restricted, for the most part, to planes perpendicular to the dc magnetic field. The presence of a space-charge density inside the gyrotropic sphere is another departure from the Mie situation, where no space-charge density exists. The second system considered, a compensated two-carrier magnetoplasma sphere (similar, in many respects, to electron-hole drops), represents a stark contrast to the single-carrier magnetoplasma. The structure of the spectra of electric and magnetic dimensional resonances of the compensated system differs in a qualitative manner from that of the single-carrier system. The internal field patterns also reflect this difference and emphasize the importance of the near-surface region in the resonant interaction of a compensated two-carrier magnetoplasma with electromagnetic fields. The disparity in the behavior of the resonance spectra of the two systems underscores the wide range of phenomena that can be described via the Ford and Werner solution of the gyrotropic-sphere problem.

## I. INTRODUCTION

In the preceding paper, Ford and Werner[1] have developed a formal solution to the problem of the scattering of a plane electromagnetic wave by a gyrotropic sphere, i.e., a sphere composed of a medium which is described by a dielectric tensor of the form

$$\vec{\epsilon} = \begin{bmatrix} \epsilon_{xx} & \epsilon_{xy} & 0 \\ -\epsilon_{xy} & \epsilon_{xx} & 0 \\ 0 & 0 & \epsilon_{zz} \end{bmatrix}. \tag{1}$$

This generalization of the problem of isotropic Mie scattering does not yield, with the exception of certain limits,[1,2] closed-form analytic expressions for the various cross sections which describe the wave-sphere interaction. Consequently, the numerical computation of the expressions given in the preceding paper forms an integral part of the total discussion of the gyrotropic sphere problem.

In this paper, we explore various aspects of the numerical solution, seeking to identify general trends and to provide physical insight into the interaction of a plane wave with a gyrotropic sphere. The gyrotropy in the examples we consider will arise from the presence of a dc magnetic field. Our attention will be focused mainly on the situation in which the magnetic field and the direction of incidence of the plane wave coincide. Under these circumstances, the incident plane wave can be resolved into two circular polarizations which interact independently with the gyrotropic sphere, and the two modes of excitation can be separately examined experimentally (see Fig. 1).

Our discussion employs examples using the parameters appropriate to spheres made from semiconductors and irradiated with microwaves. We choose this parameter range because of our own experimental interest and experience in it.[3,4] We exclude other related topics of interest, such as low-frequency helicon standing-wave resonances in metals and the behavior of the resonance spectra of semiconducting spheres in the Rayleigh-limit, because they have been previously discussed.[5-7] We emphasize those features of the resonance spectra which require the general solution of Ford and Werner for their understanding, such as the electric and magnetic dimensional resonances shown in Fig. 1; and we ignore features that are adequately characterized by expressions valid under more limited circumstances than is the Ford and Werner solution, such as plasma-shifted cyclotron resonance (PSCR).

In Sec. II, we review propagation in an unbounded gyrotropic medium and the Drude dielectric tensor elements, and we discuss the extinction cross sections for geometries of special interest. In Sec. III, we describe the interaction of an electromagnetic wave with a gyrotropic sphere made of

 

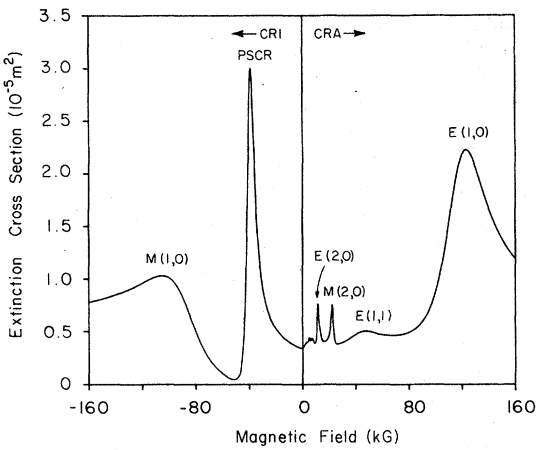


FIG. 1. Extinction cross section ($\sigma_{tot}$) for a 1.0-mm radius sphere in free space ($\epsilon_2 = 1$) as a function of magnetic field at 35 GHz. The direction of propagation of the microwaves incident on the sphere is the same as that of the dc magnetic field. The sphere consists of an $n$-type semiconductor with material parameters as follows: $\epsilon_l = 17.5$, $N = 10^{15}$ cm$^{-3}$, $\mu = 2 \times 10^5$ cm$^2$/V sec, and $m^* = 0.014\, m_e$, where $m_e$ is the free-electron mass. The dimensional resonances, marked as electric ($E$) or magnetic ($M$), are labeled according to the convention given in the text. The two linearly independent circular polarizations for incident electromagnetic radiation are plotted on the positive $B$ field side of the axis for the cyclotron-resonance-active (CRA) polarization and on the negative side for the cyclotron-resonance-inactive (CRI) polarization. A matrix size of 15 was employed in the cross-section calculation. The parameters used are typical of $n$-type InSb.

a medium having a single type of free carrier. In Sec. IV, we discuss the situation which exists when the gyrotropic sphere medium is a compensated, two-carrier magnetoplasma. Finally, in Sec. V, we consider various aspects of the computations involved in the gyrotropic sphere solution.

## II. BACKGROUND

### A. Normal modes of propagation in an unbounded medium

In the presence of a dc magnetic field $\vec{B}$, where the $\hat{z}$ direction is chosen parallel to $\vec{B}$, the dielectric tensor of an isotropic semiconductor (or an anisotropic semiconductor, if $\vec{B}$ lies along an axis of threefold or higher symmetry) takes the form given by Eq. (1). This gyrotropic tensor can be diagonalized in the coordinate system given by the three unit vectors $\hat{e}_m$:

$$\hat{e}_1 = -(1/\sqrt{2})(\hat{x} + i\hat{y}),\quad \hat{e}_{-1} = (1/\sqrt{2})(\hat{x} - i\hat{y}),\quad \hat{e}_0 = \hat{z}, \tag{2}$$

resulting in the form

$$\vec{\vec{\epsilon}} = \begin{pmatrix} \epsilon_+ & 0 & 0 \\ 0 & \epsilon_- & 0 \\ 0 & 0 & \epsilon_{zz} \end{pmatrix} = \begin{pmatrix} \epsilon_{xx} + i\epsilon_{xy} & 0 & 0 \\ 0 & \epsilon_{xx} - i\epsilon_{xy} & 0 \\ 0 & 0 & \epsilon_{zz} \end{pmatrix}. \tag{3}$$

For any given angle $\theta$ between $\vec{B}$ and the direction of propagation of the plane wave in the gyrotropic medium $\hat{k}'$, two independent polarizations may propagate. These are the normal modes of the system. Each normal mode is described by a distinct propagation constant $q$, which is related to an *effective* dielectric constant by the relationship

$$q_{1,2}^2 = (\omega^2/c^2)\epsilon_{1,2}^{\text{eff}}. \tag{4}$$

For an arbitrary angle $\theta$, the normal modes are elliptically polarized and are described by quite complicated effective dielectric constants.[8]

Two geometries are of particular interest: $\theta = 0°$ or $\hat{k}' \parallel \vec{B}$ (the Faraday geometry) and $\theta = 90°$ or $\hat{k}' \perp \vec{B}$ (the Voigt geometry). In the Faraday geometry, the normal modes are two opposite transverse circular polarizations, one (labeled "+") having the direction of its electromagnetic-wave fields $\vec{B}_1$ and $\vec{E}_1$ specified by $\hat{e}_1$, the other (labeled "−") having them specified by $\hat{e}_{-1}$. The effective dielectric constants associated with the two normal modes are $\epsilon_+$ for the "+" circular polarization and $\epsilon_-$ for the "−" circular polarization. For single-carrier gyrotropic media, the two circular polarizations are often referred to as cyclotron resonance active (CRA) or cyclotron resonance inactive (CRI) according to whether the polarization can or cannot induce cyclotron resonance of the carrier in the bulk medium. For negative carriers, the "+" polarization is the CRA polarization.

In the Voigt geometry, propagation of the normal modes is described by the effective dielectric constants

$$\epsilon_\parallel = \epsilon_{zz} \text{ and } \epsilon_\perp = (\epsilon_{xx}^2 + \epsilon_{xy}^2)/\epsilon_{xx}. \tag{5}$$

One normal mode ($\parallel$) has the electric field parallel to $\hat{z}$ (the direction of the dc magnetic field). The other normal mode ($\perp$) has the magnetic field $\vec{B}_1$ parallel to $\hat{z}$, while $\vec{E}_1$ is perpendicular to $\hat{z}$. These modes are often referred to as the ordinary Voigt (OV) and extraordinary Voight (EV) geometries, respectively.[8]

### B. Extinction cross section for particular geometries

The interaction of an electromagnetic wave with an object on which it is incident is conveniently

described in terms of extinction, absorption, and scattering cross sections. In this paper, we concern ourselves exclusively with the extinction, or total, cross section for the interaction of a plane wave with a gyrotropic sphere. The sizes of the spheres which we employ in our examples are sufficiently small for the absorption and extinction cross sections to be nearly equal and for the scattering cross section to be negligible in comparison with the other two. We limit our discussion to two geometries: the one in which the direction of propagation of the incident wave ($\hat{k}$) is parallel to $\vec{B}$, and the one in which $\hat{k}$ is perpendicular to $\vec{B}$. By way of analogy with the unbounded gyrotropic medium nomenclature, we refer to these geometries as the Faraday and the Voigt geometries, respectively.

The combination of Eqs. (FW 2.59) and (FW 3.49) from the preceding paper[1] (all equations referenced from the preceding paper by Ford and Werner will have FW prefixed to the equation number) gives a general expression for the extinction cross section of a gyrotropic sphere. For the Faraday geometry, the general expression for the extinction cross section reduces to

$$\sigma_{\text{tot}} = \frac{2\pi}{k^2}\text{Re}\left[\sum_{l=1}^{\infty}\sum_{l'=1}^{\infty}(+i)^{l'-l}[(2l'+1)(2l+1)]^{1/2}\frac{j_l(x)}{h_{l'}^{(1)}(x)}\sum_{m=\pm1}\sum_{\sigma=\pm}Z_{ll'}^{m\sigma}\times\begin{cases}\left(\dfrac{|\hat{e}_m^*\cdot\vec{E}_1|^2}{|\vec{E}_1|^2}\right), & \sigma=(-)^{l+1}\\ \dfrac{|\hat{e}_m^*\cdot\vec{B}_1|^2}{|\vec{B}_1|^2}, & \sigma=(-)^{l}\end{cases}\right]. \tag{6}$$

The sum of $m$ over $2l+1$ values in the general expression has been reduced to a sum over only two values, each of which corresponds to a circular polarization of the incident wave. Since each value of $m$ is associated with a different auxiliary eigenvalue problem (FW 3.15), the contribution of each value of $m$ to the total cross section is independent of the other. Thus, in the Faraday geometry, each circular polarization of the incident wave interacts independently with the gyrotropic sphere, producing two different resonance spectra.

For the Voigt geometry, the general expression for the extinction cross section reduces to an expression, given in Appendix A, which shows that two linear polarizations exist which interact independently with the gyrotropic sphere. One linear polarization ($\parallel$) has $\vec{E}_1$ parallel to $\hat{z}$ and $\vec{B}_1$ perpendicular to both $\hat{z}$ and $\hat{k}$. The other linear polarization ($\perp$) has $\vec{B}_1$ parallel to $\hat{z}$ and $\vec{E}_1$ perpendicular to both $\hat{z}$ and $\hat{k}$. In analogy with propagation in unbounded gyrotropic media, we refer to these linear polarizations as ordinary Voigt (OV) and extraordinary Voigt (EV), respectively.

In the dipole limit (or small-$ka$ limit),[1] where $|ka| \ll 1$ so that the gyrotropic sphere is located in time varying but spatially uniform electric and magnetic fields, any arbitrary external electric or magnetic field can be resolved into three components, labeled $m=+1, 0, -1$. Each field component interacts independently with the gyrotropic sphere so that three independent electric excitations and three independent magnetic excitations are possible. Even though a time-varying electric (or magnetic) field can not exist without the presence of a companion magnetic (or electric) field, we will, in considering compensated two-carrier magnetoplasmas, discuss electric and magnetic interactions as if they could be excited independently.

The two circular polarizations of the Faraday geometry reduce to the $m=+1$ and $-1$ cases for the electric and magnetic fields in the dipole limit. For the Voigt geometry in the dipole limit, the OV polarization, which has $\vec{E}_1 \parallel \hat{z}$, $\vec{B}_1 \perp \hat{z}$, and $\vec{B}_1 \perp \hat{k}$, excites the $m=0$ electric mode with $\vec{E}_1$ while $\vec{B}_1$ excites both the $m=+1$ and $m=-1$ magnetic modes. For the EV polarization, $\vec{B}_1$ excites the $m=0$ magnetic mode, while $\vec{E}_1$ excites the $m=+1$ and $m=-1$ electric modes.

### C. Drude dielectric tensor elements

In experiments carried out at microwave frequencies, the magnetic field is varied so as to change the values of the elements of the dielectric tensor and thus sweep through various gyrotropic sphere resonances. The dielectric tensor is related to the conductivity tensor $\vec{\sigma}$ by the expression

$$\vec{\epsilon} = \epsilon_l + 4\pi i\vec{\sigma}/\omega, \tag{7}$$

where $\epsilon_l$ is the lattice dielectric constant and $\omega$ is the frequency. The Drude expressions, which we employ throughout the paper, for the dielectric tensor elements of a semiconductor with $L$ types of carriers and an isotropic band structure are[8]

$$\epsilon_{xx} = \epsilon_l + i\sum_{l=1}^{L}\frac{\omega_{pl}^2}{\omega}\frac{\tau_l(1-i\omega\tau_l)}{(1-i\omega\tau_l)^2+(\omega_{cl}\tau_l)^2}, \tag{8}$$

$$\epsilon_{xy} = +i\sum_{l=1}^{L}\frac{\omega_{pl}^2}{\omega}\frac{\omega_{cl}\tau_l^2}{(1-i\omega\tau_l)^2+(\omega_{cl}\tau_l)^2}, \tag{9}$$

$$\epsilon_{zz} = \epsilon_l + i \sum_{l=1}^{L} \frac{\omega_{pl}^2}{\omega} \frac{\tau_l}{1 - i\omega\tau_l}, \tag{10}$$

where

$$\omega_{pl}^2 = 4\pi N_l e^2 / m_l^* \tag{11}$$

is the plasma frequency,

$$\omega_{cl} = q_l B / m_l^* c \tag{12}$$

is the cyclotron frequency, $\tau$ is the relaxation time ($\mu = e\tau/m^*$ is the carrier mobility), $q$ is the carrier charge (including the sign), $m^*$ is the effective mass, $N$ is the free carrier density, and the subscript $l$ refers to the $l$th type of carrier. Also,

$$\epsilon_{\pm} = \epsilon_l + i \sum_{l=1}^{L} \frac{\omega_{pl}^2}{\omega} \frac{\tau_l}{1 - i(\omega \pm \omega_{cl})\tau_l}. \tag{13}$$

Certain parameter ranges in the microwave region yield interesting simplifications of these expressions. For single-carrier systems in the high-field limit, where $|\omega_c| \gg \omega$, and $|\omega_c| \gg \tau^{-1}$, Eq. (13) reduces to the form

$$\epsilon_{\pm} = \epsilon_l \mp 4\pi N q c / B\omega . \tag{14}$$

This form suggests that, in considering the behavior of the extinction cross section in the Faraday geometry, $B^{-1}$ rather than $B$ is the more appropriate parameter. In the helicon limit, where $\omega_p^2/\epsilon_l\omega \gg |\omega_c| \gg \omega$ and $|\omega_c| \gg \tau^{-1}$, the expressions for $\epsilon_{\pm}$ are those given in Eq. (14) with $\epsilon_l$ omitted. In compensated, two-carrier systems (carriers are of opposite sign), we are in the Alfvén limit when $\omega_{pl}/\sqrt{\epsilon_l} \gg |\omega_{cl}| \gg 1/\tau_l$ and $\omega\tau_l \gg 1$, where $l = 1, 2$. In the Alfvén limit, we have

$$\epsilon_{\pm} \simeq \epsilon_{xx} \simeq 4\pi c^2 N(m_1^* + m_2^*)/B^2 . \tag{15}$$

This equation states that, in the Faraday geometry, the behavior of the two normal modes associated with the two independent circular polarizations is nearly identical.

## III. SINGLE-CARRIER RESONANCES

### A. Resonance spectrum

The resonance spectrum shown in Fig. 1 is an example of a spectrum one might observe as a function of magnetic field for a semiconducting sphere in the Faraday geometry. The major features of the spectrum of a gyrotropic, single-carrier magnetoplasma are magnetic dimensional resonances, electric dimensional resonances, and PSCR.

When the gyrotropic medium is characterized by low losses, i.e., $|\omega \pm \omega_c| \gg \tau^{-1}$, PSCR occurs at the magnetic field and for the polarization which satisfies the requirement[9]

$$\epsilon_{\pm} \simeq \epsilon_l - \omega_p^2/\omega(\omega \pm \omega_c) = -2 . \tag{16}$$

Although the derivation of the resonance condition (16) is, strictly speaking, valid only in the Rayleigh limit ($ka \ll 1$ and $|qa| \ll 1$), our calculations have indicated that it continues to hold for sphere sizes exceeding the Rayleigh limit but satisfying the dipole limit.

The electric and magnetic dimensional resonances are two intermeshed sets of resonances having the same general pattern of behavior. Each set of resonances consists of a fundamental resonance, labeled (1, 0), and a series of harmonics, labeled $(n, 0)$, where $n = 2, 3, 4, \ldots$. We shall refer to the fundamental and its harmonics as major resonances. In addition, each of these major resonances has a series of smaller resonances, or satellites, associated with it. The satellites are labeled $(n, m)$, where $m = 1, 2, 3, \ldots$. The electric and magnetic dimensional resonances are distinguished by using the notation $E(n, m)$ and $M(n, m)$, respectively.

In many cases of interest, all the dimensional resonances occur in the interaction of the gyrotropic sphere with the CRA polarization. In those cases, for each series of resonances, the fundamental [i.e., the (1, 0) resonance] occurs at the highest magnetic field. Its harmonics [the $(n, 0)$ resonances, with $n > 1$] occur at progressively lower fields as $n$ increases (see Figs. 2 and 3). The satellites occur on the low-field side of the major resonance with which they are associated. The electric and magnetic major resonances alternate in position. The $M(1, 0)$ resonance occurs at the highest magnetic field; the $E(1, 0)$ resonance is the next major resonance below the $M(1, 0)$. The $M(2, 0)$ resonance is below the $E(1, 0)$ resonance, and so on. This alternation of the two series is shown in Fig. 4.

With decreasing radius, the $M(1, 0)$ resonance moves to a limiting magnetic field position (which is observed in the sphere response to the CRA polarization), gradually losing its dimensional character and changing into a dimension-independent resonance in the Rayleigh limit.[2,4,10,11] The magnetic and electric harmonic and satellite resonances disappear as the radius is decreased and do not appear to merge into some dimension-independent Rayleigh-limit resonance.

Unlike $M(1, 0)$, the $E(1, 0)$ resonance is *not* associated with the Rayleigh-limit electric resonance, i.e., with the PSCR. As with all the other resonances except the $M(1, 0)$, it simply disappears as the radius of the sphere is decreased. The strengths of electric resonances grow faster than the strengths of the magnetic resonances

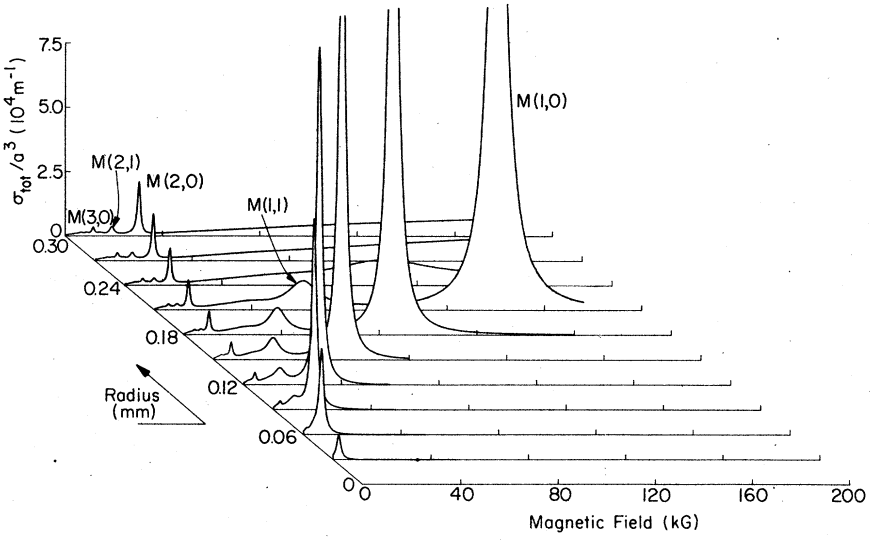


FIG. 2. Evolution of the magnetic dimensional resonance spectrum with increasing sphere radius for the Faraday geometry. The extinction cross section shown is the sum of the terms associated with $g_{l1}$ ($l$ odd) and $f_{l1}$ ($l$ even). The sphere is in free space ($\epsilon_2 = 1$) and is made of single carrier ($n$-type) material having the parameters $\epsilon_1 = 17.5$, $N = 10^{16}$ cm$^{-3}$, $\mu = 2 \times 10^5$ cm$^2$/V sec, and $m^* = 0.014\, m_e$. The incident plane wave has a frequency of 70 GHz, and its magnetic field is expressed as $\vec{B}_1 = B_1 \hat{e}_1$. The matrix size used for the calculation was 15.

with increasing radius. The $M(1, 0)$ resonance strength is roughly proportional to the fifth power of the sphere radius (Fig. 2) while the strength of the electric resonance $E(1, 0)$ is proportional to about the seventh power of the radius. The strengths of the electric resonances also increase more rapidly with frequency than the strengths of the magnetic resonances. Thus, although only magnetic dimensional resonances are observed in the low-frequency standing-wave helicon experiments,[5,6] at microwave frequencies the two types of resonances can be of the same order of magnitude, with the electric resonances often being the stronger, as is the case in Fig. 1.

The dimensional resonances are not restricted to the CRA polarization. As the sphere radius increases, the dimensional resonances, present only in the CRA polarization for small spheres, may appear in both polarizations. For the Faraday geometry, a given resonance is approximately linked to a particular value of $\epsilon_\pm a^2$. As $a$ increases, smaller values of $\epsilon_\pm$ are required for

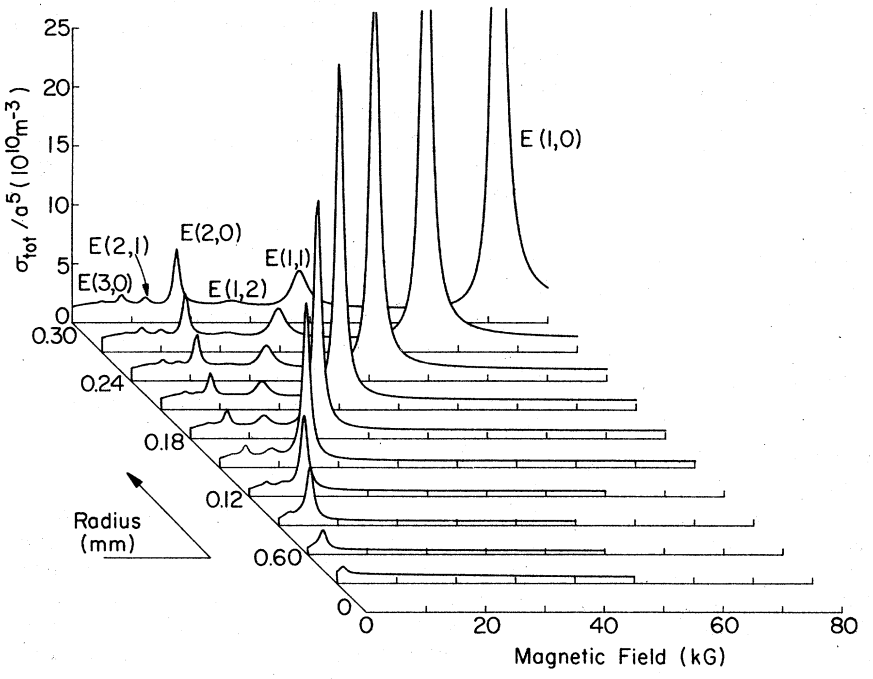


FIG. 3. Evolution of the electric dimensional resonance spectrum with increasing sphere radius for the Faraday geometry. The extinction cross section shown is the sum of the terms associated with $f_{l1}$ ($l$ odd) and $g_{l1}$ ($l$ even). The sphere and calculation parameters are identical with those listed in the caption of Fig. 2. Note the pattern of major resonances and associated satellite resonances.

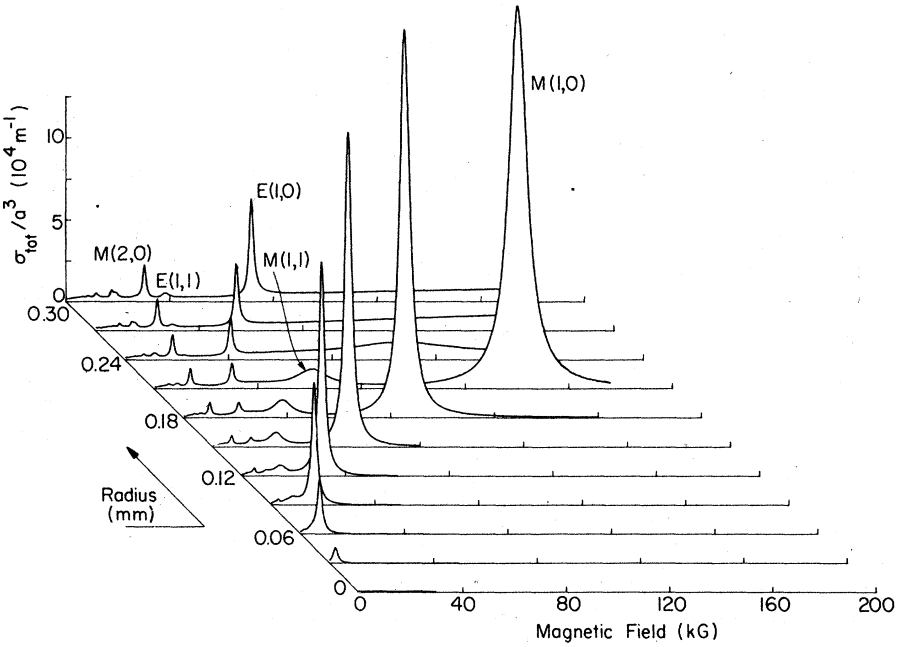


FIG. 4. Evolution of the complete dimensional resonance spectrum with increasing sphere radius for the Faraday geometry. The pattern of alternating magnetic and electric major [i.e., $(n,0)$] resonances is apparent. Note that the $E(1,0)$ resonance can be quite large, its strength exceeding that of the first harmonic magnetic resonance $M(2,0)$ for the larger sphere sizes.

the resonance to occur. Thus, for CRA excitation (which corresponds to $\epsilon_+$ for the $n$-type semiconducting spheres we are using as examples) increasing the radius moves the resonances to progressively higher fields, since, for $\omega_c > \omega$, $\epsilon_+$ decreases with increasing $B$ [see Eq. (14)]. Note, however, that $\epsilon_+$ is always larger than $\epsilon_l$. When $a$ is so large that a given resonance condition requires $\epsilon < \epsilon_l$, that resonance cannot be obtained in the CRA polarization. The resonance will then occur in the CRI polarization, for which $\epsilon < \epsilon_l$. It is clear from Eq. (13) that changing the sign of $B$ changes a given circular polarization from CRA to CRI or vice versa. Consequently, we can display both CRA and CRI responses on a single magnetic field axis, where $B > 0$ corresponds to the CRA interaction, $B < 0$ to the CRI. This is done in Fig. 1, where the sphere parameters are such that the fundamental resonance $M(1,0)$ occurs in the CRI polarization.

### B. Internal field patterns and resonance identification

We have calculated the fields within the gyrotropic sphere at the dc magnetic fields at which resonances occur. The internal field patterns in the $x$-$z$ plane are particularly helpful in characterizing the resonance interaction and labeling the resonances. The patterns shown in Figs. 5 and 6, as well as all other internal field patterns described in this paper, result from an incident circularly polarized wave propagating parallel to $\vec{B}$. The patterns shown are calculated with the incident fields $\vec{B}_1 = B_1 \hat{e}_1$ and, due to (FW 2.16), $\vec{E}_1 = iB_1 \hat{e}_1/\sqrt{\epsilon_2}$, where $\epsilon_2$ is the dielectric constant outside the sphere (in most cases, $\epsilon_2 = 1$). The decision to set $\vec{B}_1 = B_1 \hat{e}_1$ rather than $\vec{E}_1 = E_1 \hat{e}_1$ was arbitrary, based solely on the fact that the primary dimensional resonance $M(1,0)$ happens to be magnetic. The magnitudes of the arrows shown in the field patterns are proportional to the components of the fields in the plane being displayed. Each arrow is centered on the point at which the internal field is calculated.

Figure 5 shows the electric, magnetic, and generalized displacement [defined by (FW 3.1)] fields for the two fundamental resonances. The fields are calculated as complex quantities. The imaginary parts of the fields are displayed for the $M(1,0)$ resonance while the real parts of the fields are displayed for the $E(1,0)$ resonance. The manner of display is a consequence of the calculations being carried out in rotating coordinates and merits some clarification. Our coordinates are fixed by the incident microwave magnetic field, which is

$$\vec{B}_1 e^{-i\omega t} = B_1 \hat{e}_1 e^{-i\omega t} = -(B_1/\sqrt{2})(\hat{x} + i\hat{y}) e^{-i\omega t}.$$

The field plots are instantaneous "snapshots" of the $x$-$z$ plane. For $t = 0$, which is the circumstance for all the field calculations, $\vec{B}_1$ is entirely real in the $x$-$z$ plane. For a magnetic resonance, the internal magnetic field oscillates 90° out of phase with the "driving" external magnetic field

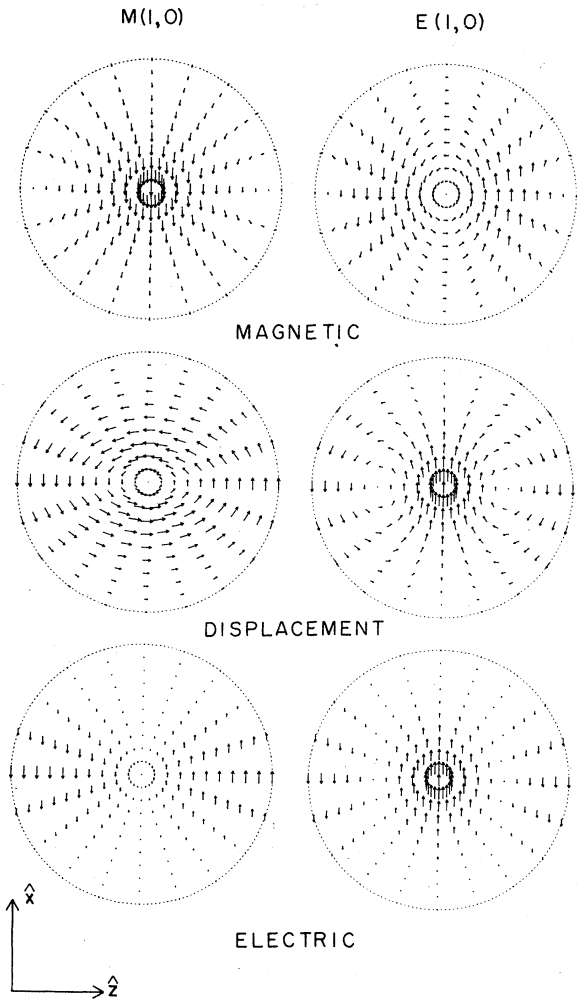


FIG. 5. Internal field patterns for the $M(1,0)$ and $E(1,0)$ resonances in the $x$-$z$ plane. The dashed line indicates the sphere boundary. The arrows are centered on the point at which the appropriate field (magnetic, displacement, or electric) was calculated. The magnitude of the arrow is proportional to the magnitude of the component of the given field in the $x$-$z$ plane. The direction of the arrow indicates the direction of the component of the field lying in the $x$-$z$ plane. The dc magnetic field lies in the $z$ direction, and the magnetic field of the incident plane wave is $\vec{B}_1 = B_1\hat{e}_1$ for both resonances. For the $M(1,0)$ resonance, the imaginary parts of the appropriate field components are plotted. For the $E(1,0)$ resonance, the real parts of the appropriate field components are plotted. All the internal field plots are calculated at the same instant of time ($t=0$) and employ resonances associated with very low-loss material parameters.

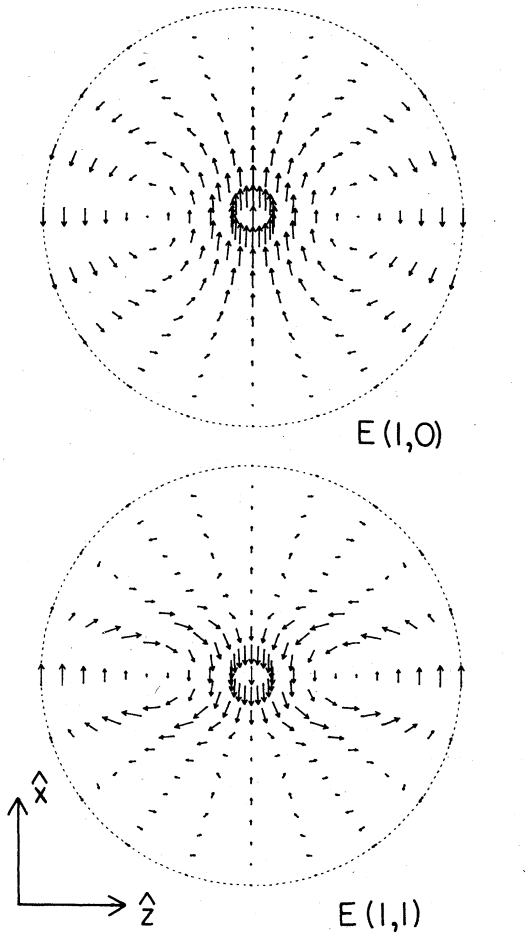


FIG. 6. Internal displacement fields for the $E(1,0)$ resonance, at the top, and its satellite, the $E(1,1)$ resonance. The magnetic field $\vec{B}_1$ of the incident plane wave is $\vec{B}_1 = B_1\hat{e}_1$. The displacement fields are plotted as described in the caption to Fig. 5. Note that the field patterns are similar along the axis (with the exception of a 180° phase shift) but differ markedly somewhat above and below the $z$ axis.

$\vec{B}_1$ and is, therefore, imaginary in the $x$-$z$ plane at $t=0$. The electric and displacement fields are induced 90° out of phase with the internal resonant magnetic field in a plane perpendicular to it. Due to the rotation of fields considered here, the electric and displacement fields also appear as imaginary in the $x$-$z$ plane. Thus, all three fields associated with the resonance appear coplanar and in phase.

The same arguments underlie the display of the fields associated with $E(n,m)$ resonances. The driving electric field is imaginary in the $x$-$z$ plane at $t=0$. The internal electric and displacement fields are coplanar and 90° out of phase with the driving field. The induced magnetic field is, in turn, 90° out of phase with those internal fields and perpendicular to them. As a result, all internal fields associated with $E(n,m)$ resonances simultaneously appear as *real* on the $x$-$z$ plane, as presented in Figs. 5 and 6.

The identification of resonances is done by

following a labeling scheme that is a simple extension of that proposed by Ford and Werner,[5] merely adding the labels $E$ and $M$ to denote the two different resonance series. We have found that the internal magnetic or the generalized displacement fields serve equally well as the basis of a labeling scheme, since both fields assume readily identifiable forms at resonance which are unique to and characteristic of the particular resonance. The electric field patterns are not readily useful as a basis for a labeling scheme due to the complex nature of the patterns, even though each resonance has a unique electric field pattern associated with it.

Examining the magnetic field patterns shown in Fig. 5, we see that the $M(1,0)$ resonance has two nodes along the $z$-axis and that the magnetic field varies through roughly $\frac{1}{2}$ cycle across the sphere along that direction. The $E(1,0)$ resonance has three nodes, or a full cycle, along the $z$ axis. The $M(2,0)$ resonance has 4 nodes, or $1\frac{1}{2}$ cycles; the $E(2,0)$, five nodes, or two cycles. The pattern can be continued indefinitely. The number of $\frac{1}{2}$-cycle variations indicates whether the resonance is electric or magnetic and what the value of the first index $n$ is. The internal displacement field pattern could also be used in such a scheme. In the case of the displacement field, the $M(1,0)$ resonance shows a $\frac{1}{2}$-cycle variation across the sphere along the $z$ axis (but antinode-to-antinode instead of node-to-node) and one node at the center. The $E(1,0)$ resonance shows a full-cycle variation in field strength, with two nodes along the $z$ axis, and so on.

The satellites associated with each of the $(n,0)$ resonances can be readily identified in the same manner. The variation in the appropriate field along the $z$ axis is the same for the satellite resonances as it is for their associated major resonance, as shown by the displacement field patterns for the $E(1,0)$ and $E(1,1)$ resonances in Fig. 6. The two resonances differ, however, off the $z$ axis. The manner in which the major resonances and their satellites differ is emphasized by the schematics for the magnetic (Fig. 7) and displacement (Fig. 8) fields. Each $(n,1)$ satellite has a field pattern which reproduces above and below the $z$ axis the pattern of field vortices that exist along the $z$ axis. The field pattern of each $(n,2)$ satellite reproduces the $z$-axis pattern twice above and below the $z$ axis. Such behavior is characteristic of the field patterns (magnetic or displacement fields) of the satellites for both types of resonances, electric and magnetic.

Along the $z$ axis, the internal magnetic field is small near the surface of the sphere for all resonances while the internal electric or displacement field is close to a maximum near the surface. This behavior is consistent with regarding the gyrotropic sphere as a dielectric cavity. At res-

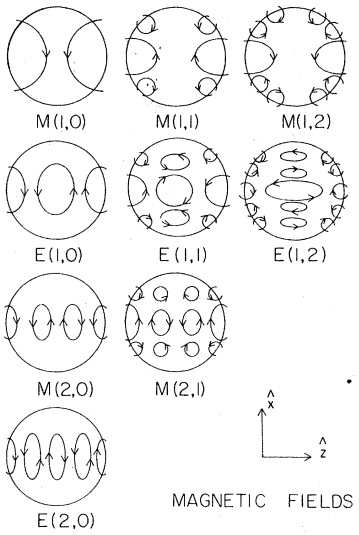


FIG. 7. Schematic diagrams of the internal magnetic field patterns for the lowest-order dimensional resonances, obtained from our internal field calculations. The schematic is intended to draw attention to the overall pattern of the magnetic field in the $x$-$z$ plane at resonance. The circular or elliptical loops are centered on field nodes, and the arrows indicate the direction of the field.

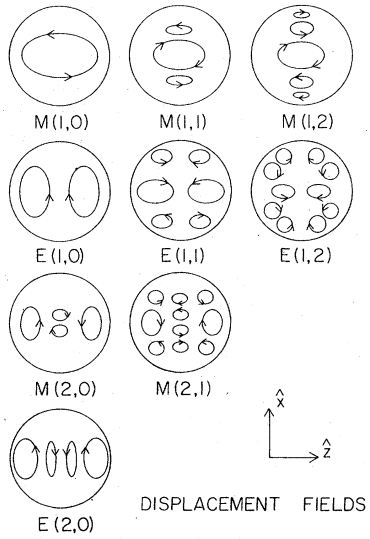


FIG. 8. Schematic diagrams of the internal displacement field patterns for the lowest order dimensional resonances, as revealed by our field calculations. Note that the central pair of loops in $M(2,0)$ and $M(2,1)$ is "equivalent" to a single, larger loop.

onance, a standing-wave pattern is set up which is the result of internal waves being reflected from the sphere surface. Upon *internal* reflection at near normal incidence, the magnetic field of these waves undergoes a phase shift of 180°, while the phase of the electric field is not shifted on reflection. Consequently, near the surface, we would expect the standing-wave magnetic field to be small (nearly a node) due to destructive interference and the electric field to be large (nearly an antinode) due to constructive interference.

### C. Comparison of the gyrotropic sphere resonances in the Faraday geometry with Mie sphere resonances

A comparison of the gyrotropic sphere calculations with isotropic (Mie) sphere results is instructive. Consider the scattered fields, which establish the externally observed behavior of the spheres. In the preceding paper, the scattered fields for both the gyrotropic and isotropic spheres have been expressed as a multipole expansion in terms of the scattered wave coefficients $f_{lm}$ and $g_{lm}$. From the fields associated with these coefficients, we can identify $f_{lm}$ and $g_{lm}$ as electric and magnetic multipole coefficients, respectively, where $l$ denotes the multipole order ($l=1$ denotes dipole, $l=2$ quadrupole, etc.). The scattered fields associated with each multipole are linearly independent, and the various cross sections for a sphere are calculated as a linear superposition of the cross sections associated with the individual multipoles.

The expressions for the scattered field coefficients for an isotropic (Mie) sphere, $f_{lm}$ and $g_{lm}$, are given in Eqs. (FW 2.44) and (FW 2.46) and are related to the usual Mie coefficients $a_l$ and $b_l$ by Eq. (FW 2.47). As the frequency, dielectric constant, or sphere size is varied, each $a_l$ Mie coefficient displays a series of electric dimensional resonances, labeled $E_{ln}$, where $l$ denotes multipole order, $n=1$ indicates the fundamental for a given multipole resonance, and $n=2,3,4,\ldots$ indicate higher harmonics. Thus, $E_{1n}$ resonances indicate electric dipole resonances; $E_{2n}$ indicate electric quadrupole resonances, and so on. Similarly, $b_l$ displays a series of magnetic Mie resonances labeled $M_{ln}$.

It is important to note that in the Mie case not only the scattered, but also the internal fields corresponding to a given multipole oscillation are linearly independent of all other multipole fields. This means that any multipole resonance can be excited independently of all other resonances of different multipole order, i.e., each multipole has separate resonance conditions. Also, the contribution to the extinction cross section associated with each multipole (i.e., each $a_l$ and $b_l$ coefficient) is always positive.

In sharp contrast to this, in the gyrotropic sphere situation, the dipole terms $f_{11}$ and $g_{11}$ together display the full set of resonances exhibited by a complete solution, including all multipole terms. The sphere resonances arise from minima in the denominators of the $Z_{ll'}^{m\sigma}$, but expressions

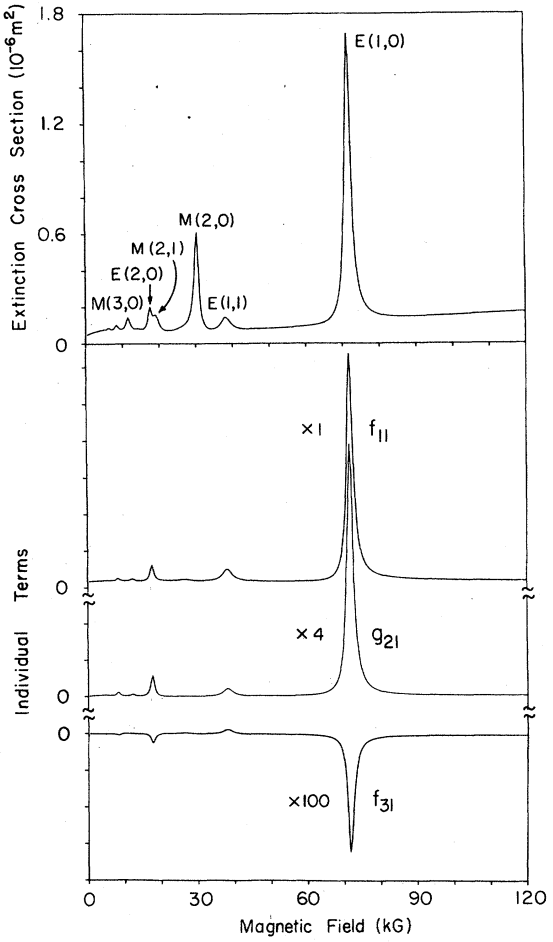


FIG. 9. Extinction cross section for a 0.3-mm radius sphere as a function of dc magnetic field. The upper part of the figure shows the extinction cross section. The lower part of the figure shows the individual contributions to the extinction cross section arising from the first three terms associated with the electric resonances. The multiplier shown for each term indicates the scale of the spectrum arising from that term with respect to the scale of the total cross section shown at the top of the figure. Note that no trace of the magnetic resonances appears in any of the individual terms displayed. Also note that the individual contributions to the total cross sections are not all positive. The calculation was performed with $\vec{B}_1 = B_1\hat{e}_1$ and a matrix size of 15 for a single-carrier magnetoplasma described by the parameters listed for Fig. 2.

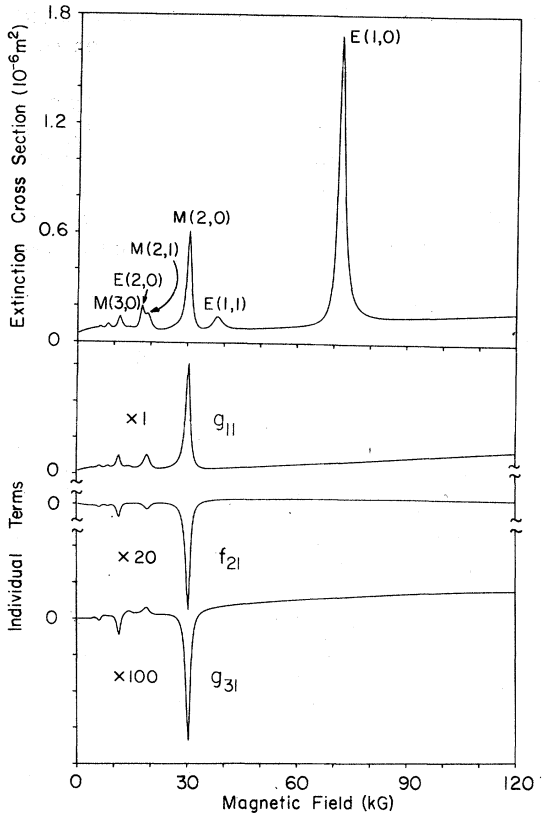


FIG. 10. Extinction cross section for a sphere with a radius of 0.3 mm as a function of dc magnetic field. The upper portion of the figure shows the extinction cross section, while the lower portion shows the individual contributions to the extinction cross section from the first three individual terms ($g_{11}$, $f_{21}$, $g_{31}$). Note that these terms make contributions (positive or negative) only to the magnetic resonances. The multiplier indicates the relationship between the scale of each individual contribution to the cross section and the scale used for plotting the extinction cross section.

(FW 3.47) and (FW 3.48) show that there are only two different denominators, corresponding to the two parities, $\sigma = +$ and $\sigma = -$, resulting from two different eigenvalue problems. Thus, the resonances that appear in $f_{11}$ also appear in all electric multipole coefficients $f_{l1}$ for $l$ odd and all magnetic multipole coefficients $g_{l1}$ for $l$ even, as shown in Fig. 9. Likewise, the resonances that appear in $g_{11}$ also appear in all $g_{l1}$ having $l$ odd and all $f_{l1}$ having $l$ even (Fig. 10). This is a consequence of the fact that the gyrotropy leads to a coupling of all multipole orders of the internal fields.[12] Also, the higher-order terms in the series for the gyrotropic sphere cross sections [Eq. (FW 2.58)] are no longer required to be positive. Consequently, an independent physical interpretation of each higher-order term is questionable. However, the total cross sections always remain positive, as required physically.

In the Mie sphere situation, magnetic multipole resonance fields have no radial electric field components at the surface of the sphere; electric multipole resonance fields have no radial magnetic field components at the surface of the sphere. For the gyrotropic sphere, on the other hand, radial components of both magnetic and electric fields appear at the sphere surface for all resonances. Consequently, our labeling of resonances as electric or magnetic is based solely upon whether the resonance occurs in the electric dipole term $f_{11}$ or the magnetic dipole term $g_{11}$, since these terms provide the dominant contributions to the cross section for the sphere sizes we are dealing with.

We now compare the calculated Mie resonance field patterns with those for the gyrotropic sphere. The $x$-$z$ sections of magnetic field for the lowest-order (fundamental) magnetic and electric gyrotropic sphere resonances (Fig. 5) and Mie sphere resonances (Fig. 11) are very similar, as is the displacement field for the gyrotropic sphere resonances in the $x$-$z$ plane when compared to the electric field of the Mie resonances in the same plane. (Note that the electric and displacement fields have identical patterns in the Mie case.) From the similarity of these, as well as higher-order Mie resonance field patterns, to those of the major gyrotropic sphere resonances, we conclude that the Mie $(1, n)$ dipole resonances correspond to the $(n, 0)$ resonances observed for the gyrotropic sphere.

Unlike the similarity noted for the magnetic and displacement fields, however, the electric fields differ radically for the gyrotropic and Mie resonances. As pointed out above, the Mie electric and displacement field patterns are identical. In the gyrotropic sphere, on the other hand, the electric field is, for the most part, restricted to planes perpendicular to the $z$ direction due to the fact that a large conductivity is associated with the direction of the dc magnetic field. The electric field can be restricted to such a plane because a volume charge density can exist inside a gyrotropic sphere. This is also in sharp contrast with the isotropic sphere case, where no volume space charge is to be found at any time.

A comparison of the internal field configurations for higher-order Mie resonances (Fig. 12) with those shown schematically in Fig. 7 emphasizes the mixing of internal fields which occurs in the gyrotropic sphere. Such a comparison indicates that the satellite $M(1, 1)$ resonance might be related to the octupole rather than the quadrupole Mie resonance. The magnetic field of $M(1, 1)$

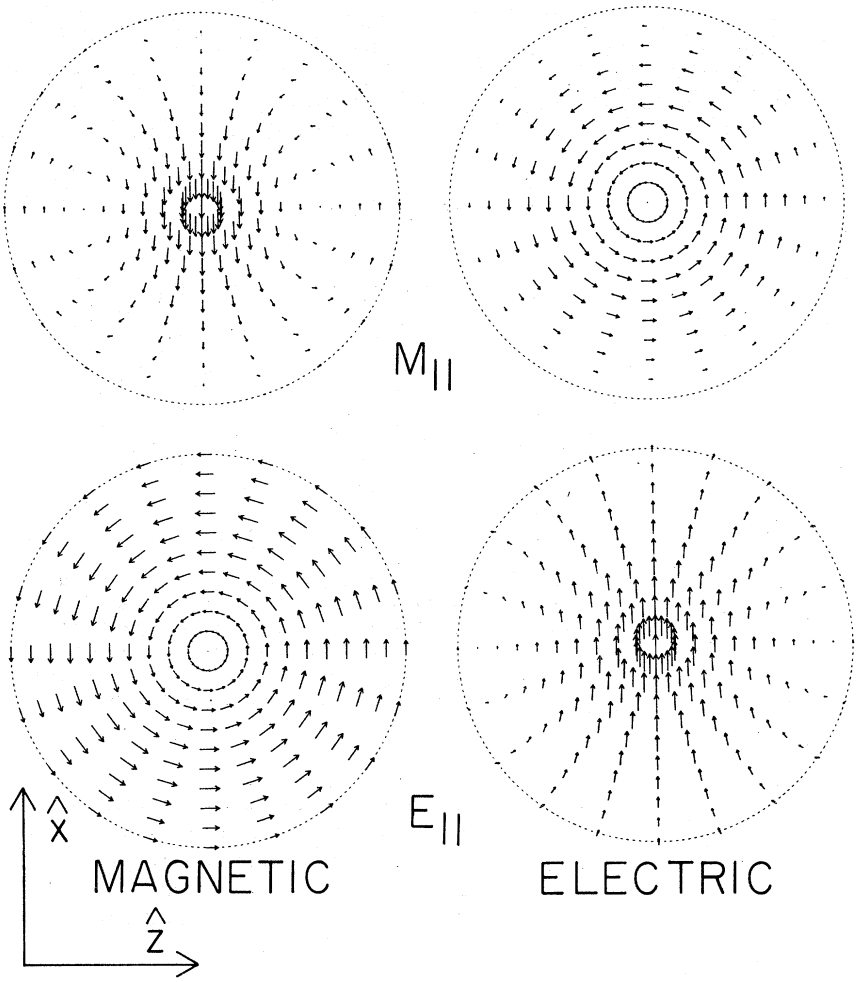


FIG. 11. Internal magnetic and electric fields for the $M_{11}$ and $E_{11}$ Mie dimensional resonances. The magnetic field of the incident plane wave is $\vec{B}_1 = B_1\hat{e}_1$, and $\vec{k}$ is parallel to $\hat{z}$. As with the gyrotropic sphere, the imaginary parts of the $M_{11}$ resonance fields and the real parts of the $E_{11}$ resonance fields are plotted on the same plane at the same instant of time.

shown in Fig. 7 can couple to a dipole scattered field, which is associated with $g_{11}$—its character along the $z$ axis is clearly dipolelike. At the same time, its resemblance to the Mie octupole field pattern suggests that it will also couple to the octupole scattered field, associated with $g_{31}$, rather than the quadrupole scattered field, associated with $g_{21}$. Such a situation is consistent with the appearance of magnetic resonances in only the $g_{lm}$ with odd $l$.

As previously mentioned, the difference between the gyrotropic and isotropic sphere problems is particularly emphasized by the fact that, while there is no induced volume charge density in an isotropic sphere, a volume space-charge density is present in the gyrotropic sphere. From Eqs. (FW 3.20), (FW 3.25), (FW 2.7), and (FW 2.3), we get an expression for the volume charge density $\rho$ at any point in the sphere

$$\rho = \epsilon_l \nabla \cdot \vec{E}_{\text{ins}}$$

$$= -\epsilon_l \sum_{\lambda,m,\sigma} i\frac{cq^2}{\omega\tilde{\epsilon}} G^{m\sigma}(\lambda) \times \sum_{l=1}^{\infty} j_l(qr) Y_{lm}(\hat{r}) \Delta^{\sigma}_{lm}(\lambda)[l(l+1)]^{-1/2}. \quad (17)$$

Figure 13 shows the charge density for a $M(1, 0)$ resonance in the $x$-$z$ plane. The pattern the charge density assumes for a $M(1, 0)$ resonance resembles an electric quadrupole. This is another illustration of internal mixing: when a resonance occurs in $g_{11}$, it will also occur in $f_{21}$, the electric quadrupole term (see Fig. 10).

### D. Empirical resonance conditions

In the perturbation treatment of the gyrotropic sphere satisfying the Rayleigh limit,[2] certain ex-

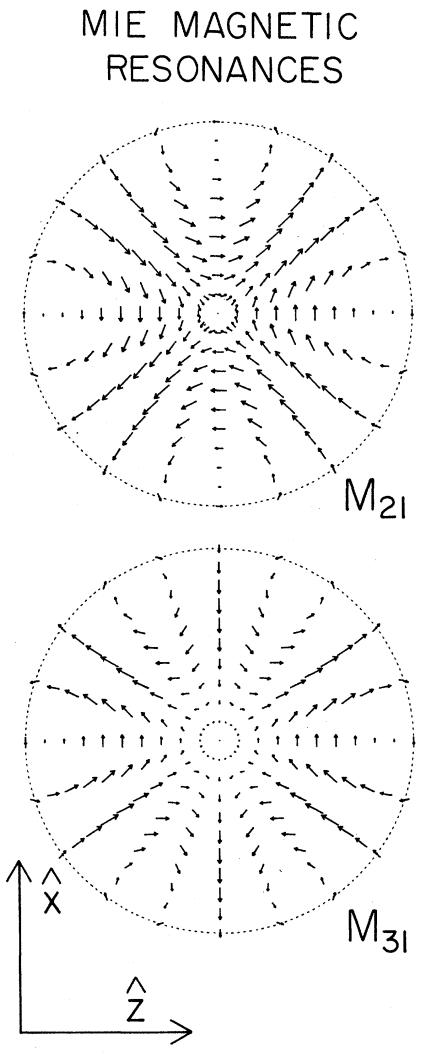


FIG. 12. Internal magnetic fields for the $M_{21}$ and $M_{31}$ Mie dimensional resonances. The magnetic field of the incident plane wave is $\vec{B}_i = B_i \hat{e}_i$ and $\vec{k}$ is parallel to $\hat{z}$. The imaginary parts of the fields are plotted.

pressions containing the principal dielectric tensor elements were developed which functioned in a manner analogous to the principal dielectric tensor elements for an infinite gyrotropic medium. The expressions were

$$\epsilon_{\pm 1}^{(\mathrm{eff})} = 2\epsilon_{\pm}\epsilon_{zz}/(\epsilon_{\pm}+\epsilon_{zz}) \tag{18}$$

and

$$\epsilon_{0}^{(\mathrm{eff})} = 2\epsilon_{+}\epsilon_{-}/(\epsilon_{+}+\epsilon_{-}), \tag{19}$$

where the subscripts ±1 and 0 refer to the components of the exciting field. In the *helicon* limit in the Faraday geometry $|\epsilon_{zz}| \gg |\epsilon_{\pm}|$, so that $\epsilon_{\pm 1}^{(\mathrm{eff})} \simeq 2\epsilon_{\pm}$. This suggests that the $\epsilon_{\pm}$ might remain an appropriate tensor element for the dimensional

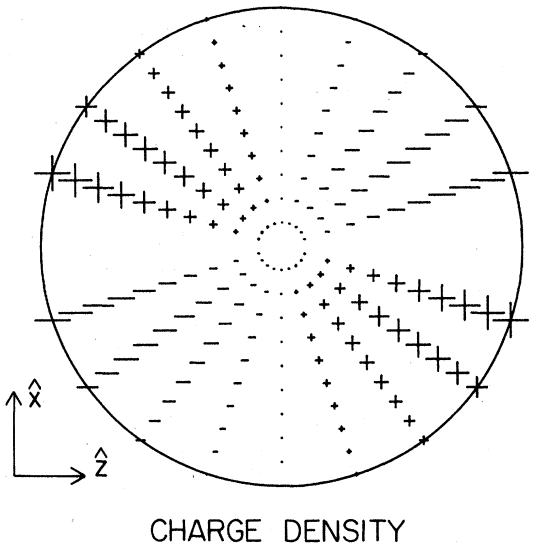


FIG. 13. Volume charge density in the $x$–$z$ plane inside a magnetoplasma sphere for a $M(1,0)$ resonance. The (+) and (–) signs shown on the figure indicate the sign of the volume charge density at the point upon which the symbol is centered. The size of the sign is proportional to the magnitude of the volume charge density at the point.

resonance discussion. Based upon this idea, we have developed empirical resonance conditions adequate for the purpose of quick identification of the major resonances. Our resonance condition for the major magnetic dimensional resonances is

$$(\omega^2 a^2/c^2)\,\mathrm{Re}\{\epsilon_p\} = n(n-\tfrac{1}{2})\pi^2 . \tag{20}$$

For the major electric dimensional resonances, our relationship is

$$(\omega^2 a^2/c^2)\,\mathrm{Re}\{\epsilon_p\} = n(n+\tfrac{1}{2})\pi^2 , \tag{21}$$

where $p$ is either "+" or "–," depending upon the polarization of the incident radiation which produces the resonance. The index $n$ is the index on the major resonances $(n, 0)$.

When the high-field-limit expressions for $\epsilon_{\pm}$ are used, the resonance positions for magnetic resonances are given by

$$B_R^M(n,0) = \frac{-4\pi Nqc}{\omega}\left(\frac{\pi^2 c^2 n(n-\frac{1}{2})}{\omega^2 a^2} - \epsilon_l\right)^{-1} . \tag{22}$$

For electric resonances, the resonance positions are given by

$$B_R^E(n,0) = \frac{-4\pi Nqc}{\omega}\left(\frac{\pi^2 c^2 n(n+\frac{1}{2})}{\omega^2 a^2} - \epsilon_l\right)^{-1} . \tag{23}$$

Note that $B_R$ can be positive or negative. A negative $B_R$ indicates that the resonance is excited via the opposite polarization to that associated

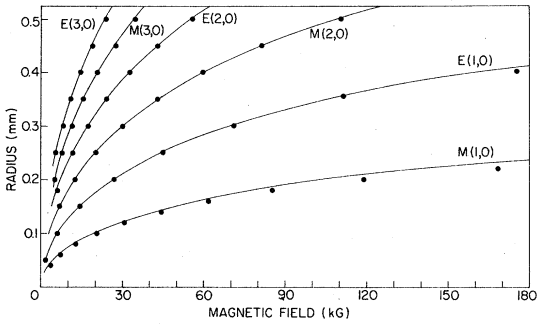


FIG. 14. Magnetic fields at which the major dimensional resonances occur for various radii. The solid lines are the resonance fields calculated via Eqs. (22) and (23). The dots represent resonance fields determined via numerical computations employing the full Ford and Werner gyrotropic sphere solution.

with $\epsilon_+$. A comparison between the resonance positions of the major resonances as calculated via the general solution (the dots in Fig. 14) and the resonance positions predicted by Eqs. (22) and (23) (solid lines) is shown in Fig. 14. The figure demonstrates the utility of Eqs. (22) and (23).

## IV. COMPENSATED, TWO-CARRIER MAGNETOPLASMA

### A. Resonance patterns

The resonance spectra exhibited by gyrotropic spheres made of compensated, two-carrier magnetoplasmas are qualitatively quite different from the resonance spectra of single-carrier magnetoplasmas. We describe the spectra seen in the dipole limit. The resonance spectra displayed for the dipole limit are calculated via the method outlined in Sec. III C of the preceding paper,[1] employing the expressions (FW 4.20) and (FW 4.21) rather than the general solution.

In the Faraday geometry, the spectra are nearly identical for $m=+1$ and $m=-1$. Consequently, we show the electric (Fig. 15) and magnetic (Fig. 16) resonance spectra for only the $m=+1$ case. We have developed no labeling scheme for the compensated, two-carrier magnetoplasma resonance spectra. The fundamental magnetic resonance, that is, the resonance which merges into a Rayleigh-limit magnetic dimension-independent resonance as the radius is decreased, is the only resonance apparent at small radii. As the radius

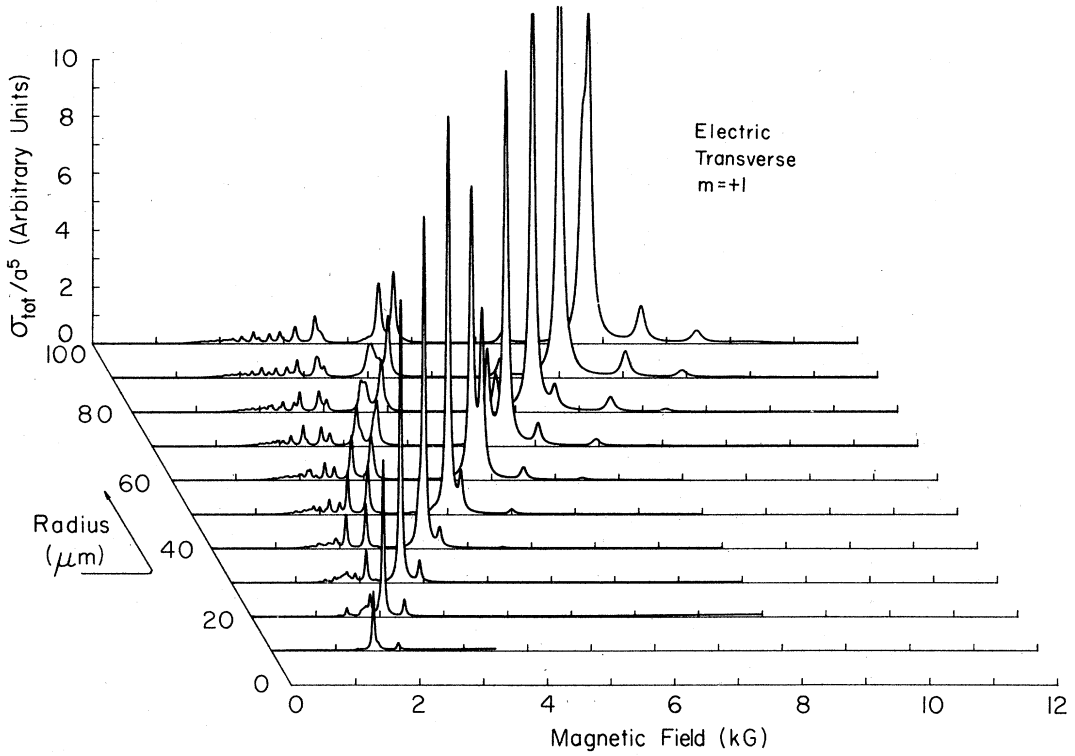


FIG. 15. Development of the dipole-limit transverse ($m=+1$) electric resonances with increasing sphere radius for a compensated, two-carrier magnetoplasma. Matrix sizes as large as 19 were used in the calculations of the extinction cross sections shown. The parameters of the semiconductor sphere were $\epsilon_1=\epsilon_2=16$, $N_h=N_e=10^{17}$ cm$^{-3}$, $\tau_h=\tau_e=5\times10^{-10}$ sec, $m_h^*=0.277\ m_e$, and $m_e^*=0.135\ m_e$, where the subscripts $e$ and $h$ refer to electron and hole parameters, respectively. The external field has a frequency of 25 GHz. The calculations were performed according to the algorithm of Sec. IV B of the preceding paper (Ref. 1). The parameters used are appropriate for electron-hole drops in Ge.

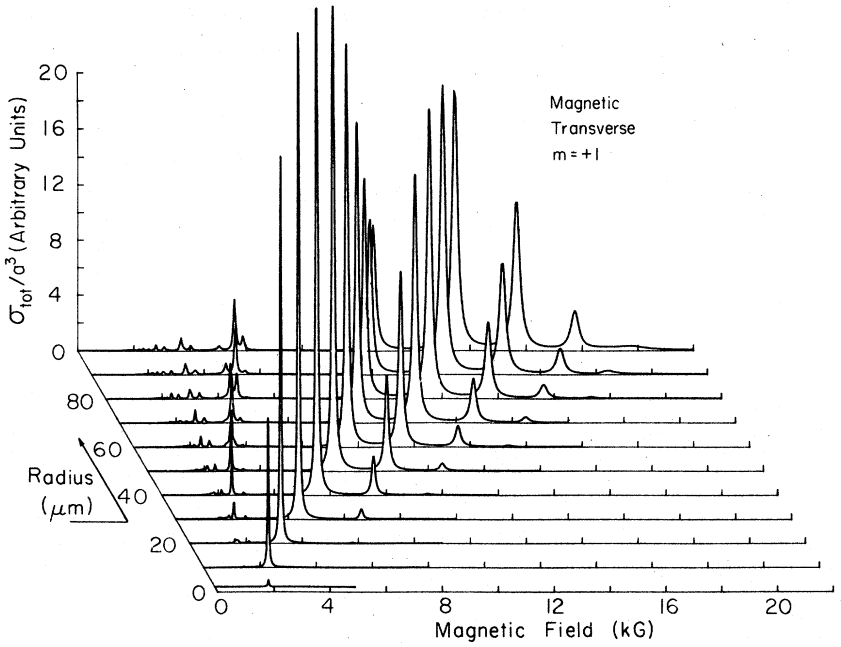


FIG. 16. Development of the dipole-limit transverse ($m=+1$) magnetic resonances with increasing sphere radius for a compensated, two-carrier magnetoplasma. Note the evolution of resonances on the high-field side of the fundamental dimensional resonance, which, as the radius is decreased, merges smoothly into a dimension-independent resonance. The parameters of the sphere are those listed for Fig. 15. For a sphere radius of 100 $\mu$m, the transverse magnetic resonances are about 100 times as strong as the transverse electric resonances (Fig. 15).

is increased, other resonances develop on the *high*-field side of the fundamental resonance (totally unlike the single-carrier situation). Eventually, the next-higher-field resonance becomes stronger than the fundamental resonance. It, in turn, will be surpassed, eventually, by the next-higher-field resonance above it. At small radii, the strength of the fundamental resonance initially varies faster than $a^3$ and then increases at a rate less than $a^3$ for larger radii. The resonance

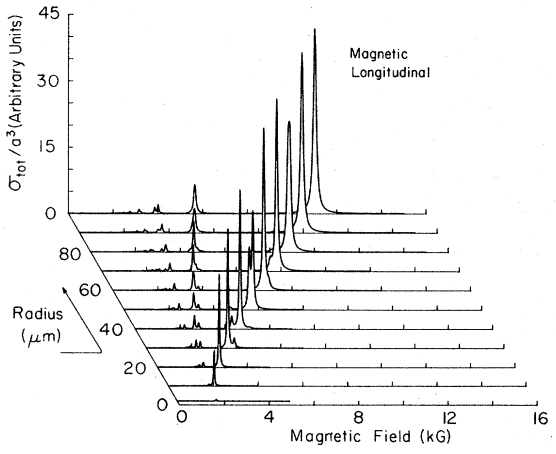


FIG. 17. Development of the dipole-limit longitudinal ($m=0$) magnetic resonances with increasing sphere radius for a compensated, two-carrier magnetoplasma. The units used on the vertical axis are the same as those of Fig. 16. The material parameters for the sphere are listed in the caption to Fig. 15.

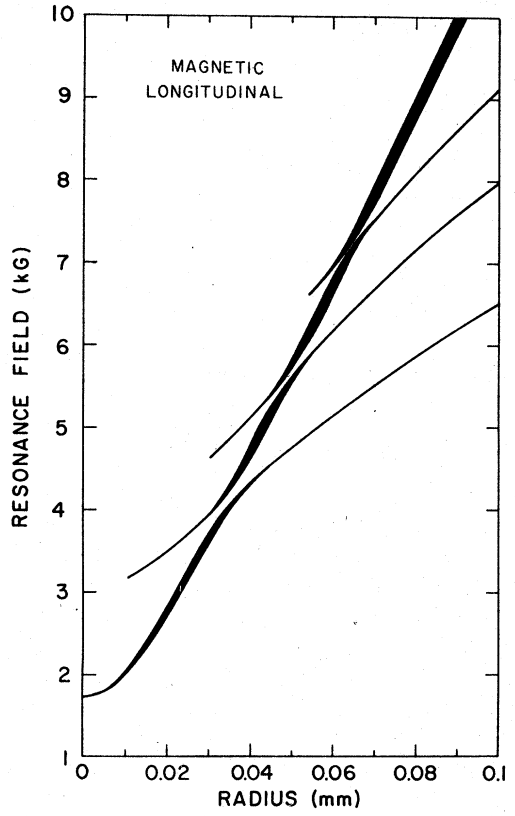


FIG. 18. Resonance field as a function of sphere radius for the prominent high-field resonances of Fig. 17, which displayed longitudinal ($m=0$) magnetic spectra. The widths of the lines suggest the relative strength of the resonances.

spectra for the electric $m=0$ (longitudinal or OV-dipole-limit) situation shows a similar pattern of resonances.

The fundamental resonance (which also merges into a Rayleigh-limit magnetic resonance with decreasing radius) for the magnetic longitudinal ($m=0$) case again does not remain the highest-field resonance (Fig. 17). A set of resonances is present which repel each other as the resonances tend to cross one another, thus keeping the fundamental resonance the lowest field resonance of the set. The behavior of the primary set of resonance fields in Fig. 17 is displayed in Fig. 18. A series of resonances exist but the resonances only have sufficient strength to be observed when their positions fall near an imaginary line which could be drawn on Fig. 18. The electric transverse situation is similar to the magnetic longitudinal situation. There are sets of resonances and not just single resonances involved in forming the primary features of the spectrum. In the electric $m=\pm1$ case, though, the resonances in the set are easily visible at higher fields before they interact with another resonance in the set (Fig. 15). Also, the fundamental electric resonances, unlike the magnetic resonances, do not merge into Rayleigh-limit resonances as the radius is reduced.

### B. Internal field patterns

The internal field patterns bear out the striking dissimilarity between the one- and two-carrier magnetoplasmas. As Figs. 19 and 20 show, the fields and charge densities near the surface are extremely important. [The field patterns are for the magnetic ($m=+1$) fundamental resonance and were calculated employing the full gyrotropic

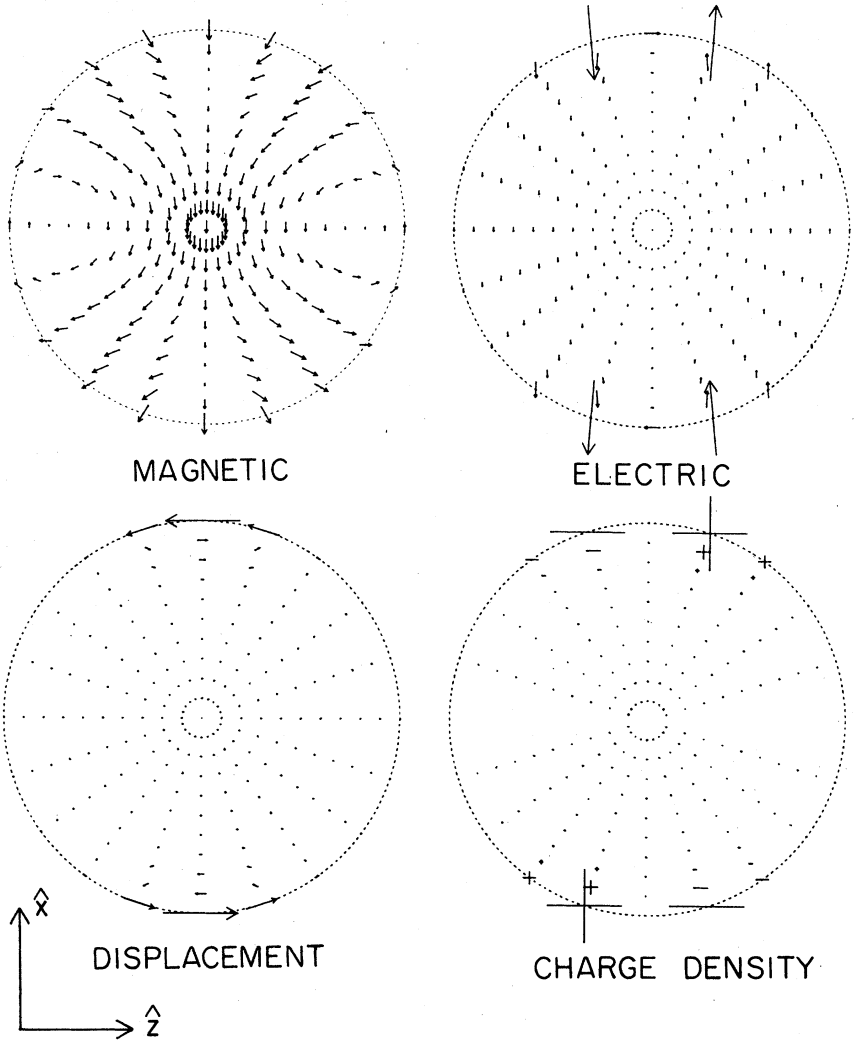


FIG. 19. Internal electric, magnetic, and displacement fields and volume charge density for the fundamental resonance of a compensated two-carrier magnetoplasma in the $x$-$z$ plane. The magnetic field of the incident plane wave has the form $\vec{B}_1 = B_1 \hat{e}_1$. The imaginary components of the internal fields and charge density are plotted. Note that electric and displacement fields and the volume charge density are most intense near the surface of the sphere.

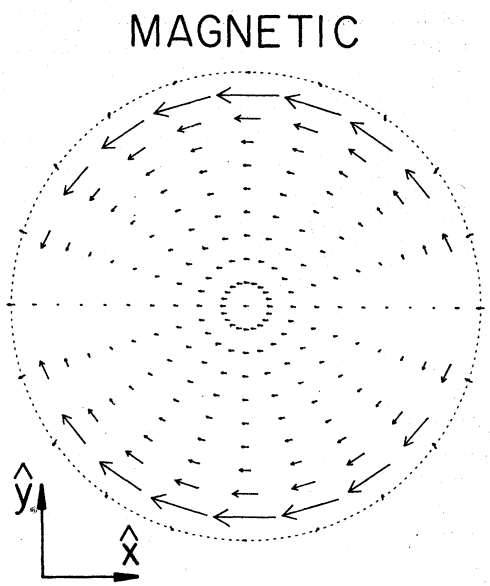


FIG. 20. Internal magnetic field for the fundamental resonance of a compensated two-carrier magnetoplasma in the $x$-$y$ plane. The magnetic field of the incident plane wave has the form $\vec{B}=B_1\hat{e}_1$. The figure shows the imaginary component of the internal field. The largest magnetic field component shown is about $6\frac{1}{2}$ times larger than the largest magnetic field component shown in the $x$-$z$ plane (Fig. 19).

solution.] In the $x$-$z$ plane, the magnetic field pattern of the fundamental resonance is similar to that of the $M(1,0)$ resonance. The magnetic field patterns of all the resonances above the fundamental look very similar to this pattern in the $x$-$z$ plane. The electric field is again, for the most part, restricted to the plane perpendicular to the dc magnetic field, but it only has significant magnitude near the surface. The field patterns suggest that for compensated two-carrier systems the resonance spectra may be extraordinarily sensitive to the near-surface region of the sphere, since all the fields are weak near the center of the sphere and much stronger near the sphere surface. [Note the magnetic field pattern in the $x$-$y$ plane shown in Fig. 20. The magnetic field in the $x$-$y$ plane is significantly stronger than in the $x$-$z$ plane.]

## V. NUMERICAL SOLUTION OF THE GYROTROPIC SPHERE PROBLEM

### A. Numerical algorithm

The algorithm used for most of the numerical computations described in this paper differs from the technique employing the $Z_{ll'}^{m\sigma}$ (FW 3.46), which was outlined in Sec. III C of the preceding paper.[1] Instead, the set of $N$ homogeneous equations (FW 3.40) were solved for the $G_k^{m\sigma}$ using Gaussian elimination with iterative improvement.[13] The $G_k^{m\sigma}$ thus determined were substituted directly into Eqs. (FW 3.42) and (FW 3.43) to determine $f_{lm}$ and $g_{lm}$. Sums over $l$ from 1 to $N$ were then used in the calculation of the desired cross section [Eqs. (FW 2.54), (FW 2.57), or (FW 2.58)].

The auxiliary eigenvalue problem (FW 3.15) was modified to read

$$\sum_{l'=1}^{\infty}(\Re_{ll'}^{m\sigma}\tilde{W}+i\tilde{\gamma}\Im_{ll'}^{m\sigma}-\lambda'\delta_{ll'})d_{l'm}^{\sigma}=0\,,\quad l=1,2,3,\ldots \tag{24}$$

The eigenvalues $\lambda'$ were then substituted in the expression

$$q^2=[\tilde{\epsilon}/(1-i\lambda')]\omega^2/c^2 \tag{25}$$

to determine the $q$ associated with each value of $\lambda'$. This modification removed severe computational difficulties which occurred when $\tilde{W}$ neared zero. The modified auxiliary eigenvalue problem, which involves a general complex matrix of size $N$, was solved via EISPACK[14] routines certified for CDC 6000-series computers.

The internal fields, given by Eqs. (FW 3.24)–(FW 3.36), were calculated by truncating all sums with the first $N$ terms. Specifically, the sums in Eqs. (FW 3.24)–(FW 3.26) over all the values of $\lambda$ included the $N$ values of $\lambda$ given by the truncated eigenvalue problem (FW 3.15); and the sums on $l$ in Eqs. (FW 3.18)–(FW 3.20), (FW 3.22), and (FW 3.23) were terminated at $l=N$.

With $N=19$, the calculation of the extinction cross section of a gyrotropic sphere for a given dc magnetic field required roughly 13 sec on a CDC 6500 computer; with $N=15$, the calculation was done in about 7 sec. Completion of the calculation of the internal fields at all the positions on a 201-point grid required approximately 500 sec of computer time with $N=13$.

### B. Convergence of the numerical algorithm

The algorithm used in the numerical computation has demonstrated rapid convergence with increasing matrix size (the order of the matrix is $N$) in calculations of all the cross sections (absorption, scattering, and extinction) and of the internal fields. Figure 21 demonstrates the behavior of the calculated extinction cross section as a function of $N$ for a single-carrier magnetoplasma sphere. As a general rule of thumb, calculations of the cross sections and internal fields of a single-carrier magnetoplasma sphere require a smaller value of $N$ to obtain a given degree of

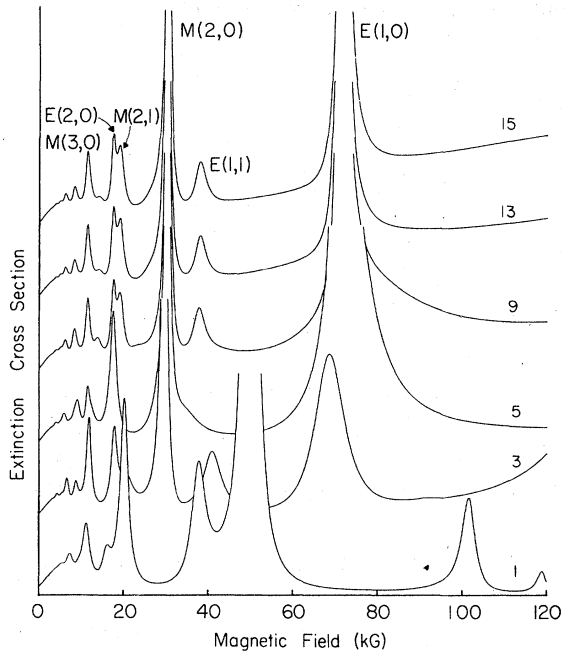


FIG. 21. Development of the calculated resonance spectra for a single-carrier magnetoplasma sphere with increasing matrix size. The sphere parameters used are those listed under Fig. 2; the sphere radius is 0.3 mm. The matrix size is indicated on the right-hand side.

accuracy than do such calculations for a compensated, two-carrier magnetoplasma sphere of the same size. Also, calculations of the internal fields for a sphere require larger values of $N$ than calculations of cross sections of the same sphere. As the radius of a sphere is increased, the size of $N$ required for the calculation increases. Under all circumstances tested to date, all failures of the numerical algorithm have been catastrophic, resulting in "hash," or noise, in the extinction cross section plotted as a function of either magnetic field or frequency.

The rapid convergence of this algorithm with increasing $N$ is due to the selection of eigenvalues made by the auxiliary eigenvalue problem (FW 3.15). In fact, the extinction cross section can be accurately calculated with $N=1$ for magnetoplasma spheres which are small enough to satisfy the Rayleigh-limit criteria. (See Appendix B for an analytic demonstration of this fact.) The convergence of this algorithm is all the more impressive in light of the fact that another approach (described in Sec. III D of the preceding paper[1]) required $N>30$ for the calculation of the extinction cross section of a sphere satisfying the Rayleigh-limit criteria.

## VI. CONCLUDING REMARKS

The preceding discussion has covered only a small portion of the interactions that can be described by Ford and Werner's solution.[1] Its focus has been determined by the experimental interest[3,4,15] that has been manifested in the interaction of microwaves with gyrotropic spheres. Also, limitations of the numerical algorithm employed and computer time available have defined the upper limit to the radii of spheres which we have investigated in this paper.

## ACKNOWLEDGMENTS

The authors wish to thank G. W. Ford and S. A. Werner for many stimulating discussions and for their continued interest in the progress of this work. The support of NSF Grants No. DMR 76-00889A1 and No. DMR 77-00034 is gratefully acknowledged.

## APPENDIX A: EXTINCTION CROSS SECTION FOR VOIGHT GEOMETRY

For the Voigt geometry, the general expression for the extinction cross section, given by the combination of Eqs. (FW 2.59) and (FW 3.49), can be reduced to the form

$$\sigma_{\rm tot}=\sigma_{\rm tot}^{\rm OV}+\sigma_{\rm tot}^{\rm EV}, \tag{A1}$$

where $\sigma_{\rm tot}^{\rm OV}$ and $\sigma_{\rm tot}^{\rm EV}$ are the contributions to $\sigma_{\rm tot}$ from the OV and EV components of the incident plane wave.

The contribution to the extinction cross section from the OV component of the incident plane wave is

$$\sigma_{\rm tot}^{\rm OV}=\frac{4\pi}{k^2}\sum_{l=1}^{\infty}\sum_{l'=1}^{\infty}\sum_{m=-\min(l,l')}^{\min(l,l')}\mathrm{Re}\left\{(-1)^{l-l'}\frac{j_l(x)}{h_{l'}^{(1)}(x)}\left[\frac{(2l+1)(2l'+1)}{ll'(l+1)(l'+1)}\frac{(l-m)!\,(l'-m)!}{(l+m)!\,(l'+m)!}\right]^{1/2}\sum_{\sigma=\pm}Z_{ll'}^{m\sigma}\right\}$$

$$\times\begin{cases}-\dfrac{(l+m)!!\,(l'+m)!!}{(l-m-1)!!\,(l'-m-1)!!}\dfrac{|E_z|^2}{|\vec{E}_1|^2}, & (l'-m)\text{ odd and }(l-m)\text{ odd},\ \sigma=(-)^{l+1}\\[2ex] m^2\dfrac{(l+m-1)!!\,(l'+m-1)!!}{(l-m)!!\,(l'-m)!!}\dfrac{|B_\perp|^2}{|\vec{B}_1|^2}, & (l'-m)\text{ even and }(l-m)\text{ even},\ \sigma=(-)^{l}\\[2ex] 0, & (l'-m)\text{ odd and }(l-m)\text{ even},\\[2ex] 0, & (l'-m)\text{ even and }(l-m)\text{ odd},\end{cases} \tag{A2}$$

where $\vec{E}_1 = E_z\hat{z} + \vec{E}_\perp\hat{u}_\perp$, $\vec{B}_1 = B_z\hat{z} + B_\perp\hat{u}_\perp$, $\vec{k} = k\hat{k}$, $\hat{z}\times\hat{k} = \hat{u}_\perp$, and $\min(l, l')$ means the smaller of $l$ and $l'$.

The contribution to the extinction cross section from the EV component of the incident plane wave is

$$\sigma_{\rm tot}^{\rm EV} = \frac{4\pi}{k^2}\sum_{l=1}^{\infty}\sum_{l'=1}^{\infty}\sum_{m=-\min(l,l')}^{\min(l,l')} \mathrm{Re}\left\{(-1)^{l-l'}\frac{j_l(x)}{h_{l'}^{(1)}(x)}\left[\frac{(2l+1)(2l'+1)}{ll'(l+1)(l'+1)}\frac{(l-m)!\,(l'-m)!}{(l+m)!\,(l'+m)!}\right]^{1/2}\sum_{\sigma=\pm} Z_{ll'}^{m\sigma}\right\}$$

$$\times\begin{cases} m^2\dfrac{(l+m-1)!!\,(l'+m-1)!!}{(l-m)!!\,(l'-m)!!}\dfrac{|E_\perp|^2}{|\vec{E}_1|^2}, & (l'-m)\text{ even and }(l-m)\text{ even},\ \sigma=(-)^{l+1}\\ \dfrac{(l+m)!!\,(l'+m)!!}{(l-m-1)!!\,(l'-m-1)!!}\dfrac{|B_z|^2}{|\vec{B}_1|^2}, & (l'-m)\text{ odd and }(l-m)\text{ odd},\ \sigma=(-)^l\\ 0, & (l'-m)\text{ odd and }(l-m)\text{ even},\\ 0, & (l'-m)\text{ even and }(l-m)\text{ odd}. \end{cases} \tag{A3}$$

Thus, the OV and EV linear polarizations interact independently with the gyrotropic sphere, since each polarization is associated with a different parity of $\sigma$ for any particular value of $m$. This is due to the fact that every combination of $m$ and $\sigma$ corresponds to a different eigenvalue problem (FW 3.15) and thus produces a sphere response different from that of the other parity.

## APPENDIX B: EQUIVALENCE OF $N=1$ EXPRESSIONS AND PERTURBATION SOLUTION RESULTS IN RAYLEIGH LIMIT

In getting the numerical solution to the gyrotropic sphere problem, various infinite sums are terminated after $N$ terms. In this appendix, we show that, for $N=1$, the truncated gyrotropic sphere solution yields the perturbation-theory expressions derived by Ford, Furdyna, and Werner[2] for power absorbed by a gyrotropic sphere.

With $N=1$, the auxiliary eigenvalue problem (FW 3.15) becomes

$$\left(\mathfrak{M}_{11}^{m\sigma} + i\frac{\tilde{\gamma}}{\tilde{W}}\mathfrak{N}_{11}^{m\sigma} - \lambda\right)d_{1m}^{\sigma} = 0. \tag{B1}$$

We set $d_{1m}^{\sigma} = 1$ and, using Eqs. (FW 3.16) and (FW 3.17), evaluate $\mathfrak{M}_{11}^{m\sigma}$ and $\mathfrak{N}_{11}^{m\sigma}$ to get

$$\lambda = \begin{cases} \dfrac{m}{2}\left(1 + i\dfrac{m\tilde{\gamma}}{\tilde{W}}\right), & \sigma = -\\ \dfrac{m}{2} + i\dfrac{\tilde{\gamma}}{5\tilde{W}}(4 - \tfrac{7}{2}m^2), & \sigma = +. \end{cases} \tag{B2}$$

Then, utilizing Eqs. (FW 3.12) and (B.2), we find that

$$q^2 = \begin{cases} \dfrac{\omega^2}{c^2}\epsilon_m^{(\rm eff)}, & \sigma = -\\ \dfrac{\omega^2}{c^2}\dfrac{10\epsilon_+\epsilon_-\epsilon_{zz}}{\epsilon_{zz}(\epsilon_+ + \epsilon_-) + 8\epsilon_+\epsilon_-}, & m = 0,\ \sigma = +\\ \dfrac{\omega^2}{c^2}\dfrac{2\epsilon_+\epsilon_-\epsilon_{zz}}{\frac{1}{2}\epsilon_{zz}[(\frac{9}{5}+m)\epsilon_- + (\frac{9}{5}-m)\epsilon_+] + \frac{1}{5}\epsilon_+\epsilon_-}, & \\ & m = \pm 1,\ \sigma = + \end{cases} \tag{B3}$$

where the $\epsilon_m^{(\rm eff)}$ are defined by Eqs. (18)–(19).

Considering only the $\sigma = -$ case, we use Eqs. (FW 3.37) and (FW 3.34) to arrive at the expression

$$g_{1m} = \frac{x^2 j_1(x)}{4\pi i}\frac{Y_1^{m-}(\lambda)}{X_1^{m-}(\lambda)}r_1^{m-}, \tag{B4}$$

where $x = ka$. The dipole-limit expressions (FW 4.11) and (FW 4.12) for $Y_l^{m\sigma}(\lambda)$ and $X_l^{m\sigma}(\lambda)$, coupled with Eqs. (FW 2.29) and (FW 3.36), reduce Eq. (B4) to

$$g_{1m} = -i\left(\frac{3}{8\pi}\right)^{1/2}\frac{j_1(x)}{h_1^{(1)}(x)}\sum_{m=-1}^{+1}\frac{j_2(y)}{j_0(y)}(\hat{e}_m^*\cdot\vec{B}), \tag{B5}$$

where $y = qa$. Employing Eq. (FW 4.32), we find that, in the Rayleigh limit,

$$g_{1m} = \frac{x^3}{15(24\pi)^{1/2}}\sum_{m=-1}^{+1}\frac{y^2}{1 - \frac{2}{21}y^2}(\hat{e}_m^*\cdot\vec{B}). \tag{B6}$$

The magnetic dipole contribution to the extinction cross section is, according to Eqs. (FW 2.58) and (FW 2.16),

$$\sigma_{\rm tot}^M = \left(\frac{4\pi}{k}\right)^2\mathrm{Re}\left(\sum_{m=-1}^{+1} g_{1m}\frac{\vec{Y}_{11}^m(\hat{k})\times\hat{k}\cdot\vec{B}_1^*}{|\vec{B}_1|^2}\right)$$

$$= \frac{2\pi}{15}\frac{ka^5\omega^2}{c^2}\sum_{m=-1}^{+1}\mathrm{Im}\left(\frac{\epsilon_m^{(\rm eff)}}{1 - \frac{2}{21}(a\omega/c)^2\epsilon_m^{(\rm eff)}}\right)\times\frac{|\hat{e}_m\cdot\vec{B}_1^*|^2}{|\vec{B}_1|^2}. \tag{B7}$$

Now, the incident intensity of the plane wave is

$$\hat{k}\cdot\vec{S}_{\rm inc} = \frac{\omega}{8\pi k}|\vec{B}_1|^2 = \frac{c^2 k}{8\pi\omega}|\vec{E}_1|^2, \tag{B8}$$

so that the power absorbed by the sphere from the external magnetic field, which is $\sigma_{\rm tot}^M$ multiplied by the incident intensity, is

$$\mathcal{P}^M = \frac{a^5\omega^3}{60c^2}\sum_{m=-1}^{+1}\mathrm{Im}\left(\frac{\epsilon_m^{(\rm eff)}}{1 - \frac{2}{21}(a\omega/c)^2\epsilon_m^{(\rm eff)}}\right)|\hat{e}_m\cdot\vec{B}_1^*|^2, \tag{B9}$$

which agrees with the Rayleigh-limit perturbation

result of Ford, Furdyna, and Werner.[2]

Returning to the $\sigma = +$ case, we use Eqs. (FW 3.37) and (FW 3.34) to get

$$f_{1m} = \frac{x^2 j_1(x)}{4\pi i} \frac{Y_1^{m+}(\lambda)}{X_1^{m+}(\lambda)} \gamma_1^{m+} . \tag{B10}$$

By replacing $\alpha_1(y)$ and $j_1(y)$ in the dipole-limit expressions (FW 4.11) and (FW 4.12) for $Y_l^{m\sigma}(\lambda)$ and $X_l^{m\sigma}(\lambda)$ with the first two terms in their series expansions (FW 4.32) and (FW 4.33), we get a Rayleigh-limit expression

$$\frac{Y_1^{m+}(\lambda)}{X_1^{m+}(\lambda)} = \frac{2 - 2c^2q^2/\omega^2\epsilon_2 - (c^2q^2/\omega^2\tilde{\epsilon})\Delta_{1m}^{+}(\lambda) - \frac{1}{5}a^2q^2}{2 + c^2q^2/\omega^2\epsilon_2 - (c^2q^2/\omega^2\tilde{\epsilon})\Delta_{1m}^{+}(\lambda) - \frac{1}{5}a^2q^2} , \tag{B11}$$

where

$$\Delta_{1m}^{+}(\lambda) = \tfrac{1}{5}(3m^2 - 2)\tilde{\gamma} + im\tilde{W} . \tag{B12}$$

Equation (B11) reduces to

$$\frac{Y_1^{m+}(\lambda)}{X_1^{m+}(\lambda)} \simeq 1 - \frac{3\epsilon_m}{2\epsilon_2 + \epsilon_m(1 - \frac{1}{5}\epsilon_2\omega^2a^2/c^2)} . \tag{B13}$$

Thus, in the Rayleigh limit, Eq. (B10) becomes

$$f_{1m} = \frac{-x^3}{(24\pi)^{1/2}} \sum_{m=-1}^{+1} \left[ 1 - \frac{3\epsilon_m}{2\epsilon_2 + \epsilon_m(1 - \frac{1}{5}\epsilon_2\omega^2a^2/c^2)} \right] \times (\hat{e}_m^* \cdot \vec{E}_1) . \tag{B14}$$

The electric dipole contribution to the extinction cross section is

$$\sigma_{\text{tot}}^{E} = -\left(\frac{4\pi}{k}\right)^2 \text{Re}\left( \sum_{m=-1}^{+1} \frac{f_{1m} \vec{Y}_{11}^{m}(\hat{k}) \times \hat{k} \cdot \vec{E}_1^*}{|\vec{E}_1|^2} \right)$$

$$= 2\pi k a^3 \,\text{Im}\left[ \sum_{m=-1}^{+1} \left( 1 - \frac{3\epsilon_m}{2\epsilon_2 + \epsilon_m(1 - \frac{1}{5}\epsilon_2\omega^2a^2/c^2)} \right) \times \frac{|\hat{e}_m^* \cdot \vec{E}_1|^2}{|\vec{E}_1|^2} \right] . \tag{B15}$$

Again, the power absorbed from the external electric field, which is $\sigma_{\text{tot}}^{E}(\hat{k} \cdot \vec{S}_{\text{inc}})$, is

$$\mathcal{P}^{E} = \frac{\epsilon_2 \omega a^3}{4} \,\text{Im}\left[ \sum_{m=-1}^{+1} \left( 1 - \frac{3\epsilon_m}{2\epsilon_2 + \epsilon_m(1 - \frac{1}{5}\epsilon_2\omega^2a^2/c^2)} \right) \times |\hat{e}_m^* \cdot \vec{E}_1|^2 \right] , \tag{B16}$$

which is identical to the Rayleigh-limit result of Ford, Furdyna, and Werner[2] when the dielectric constant outside the sphere is $\epsilon_2$ instead of 1.

---

*Present address: Thomas More College, P. O. Box 85, Ft. Mitchell, Ky. 41017.

[1]G. W. Ford and S. A. Werner, preceding paper, Phys. Rev. B 18, 6752 (1978).
[2]G. W. Ford, J. K. Furdyna, and S. A. Werner, Phys. Rev. B 12, 1452 (1975).
[3]J. R. Dixon and J. K. Furdyna, Phys. Lett. 54A, 59 (1975).
[4]T. A. Evans and J. K. Furdyna, Phys. Rev. B 8, 1461 (1973).
[5]G. W. Ford and S. A. Werner, Phys. Rev. B 8, 3702 (1973).
[6]S. A. Werner, T. K. Hunt, and G. W. Ford, Solid State Commun. 14, 1217 (1974).
[7]J. R. Dixon and J. K. Furdyna, in *Proceedings of the 13th International Conference on the Physics of Semiconductors*, edited by F. G. Fumi (North-Holland, Amsterdam, 1976), p. 918.
[8]E. D. Palik and J. K. Furdyna, Rep. Prog. Phys. 33, 1193 (1970).
[9]F. L. Galeener, Phys. Rev. Lett. 22, 1292 (1969).
[10]F. L. Galeener, T. A. Evans, and J. K. Furdyna, Phys. Rev. Lett. 29, 728 (1972).
[11]J. R. Dixon and J. K. Furdyna, Phys. Rev. B 13, 4626 (1976).
[12]R. S. Markiewicz, Phys. Rev. B 10, 1766 (1974); Phys. Rev. B (to be published).
[13]G. Forsythe and C. B. Moler, *Computer Solution of Linear Algebraic Systems* (Prentice-Hall, Englewood Cliffs, N. J., 1967).
[14]B. S. Garbow, J. M. Boyle, J. J. Dongarra, and C. B. Moler, *Matrix Eigensystem Routines—EISPACK Guide Extension* (Springer-Verlag, Berlin, 1977); B. T. Smith, J. M. Boyle, B. S. Garbow, Y. Ikebe, V. C. Klema, and C. B. Moler, *Matrix Eigensystem Routines—EISPACK Guide* (Springer-Verlag, Berlin, 1974).
[15]R. S. Markiewicz, J. P. Wolfe, and C. D. Jeffries, Phys. Rev. Lett. 32, 1357 (1974); 34, 59 (1975).